JACS
JOURNAL OF THE AMERICAN CHEMICAL SOCIETY

Article

pubs.acs.org/JACS

Enhanced Activity and Acid pH Stability of Prussian Blue-type Oxygen Evolution Electrocatalysts Processed by Chemical Etching

Lijuan Han,[†] Pengyi Tang,[‡,§] Álvaro Reyes-Carmona,[†] Bárbara Rodríguez-García,[†] Mabel Torréns,[†] Joan Ramon Morante,[§] Jordi Arbiol,[‡,∥] and Jose Ramon Galan-Mascaros*[,†,∥]

[†]Institute of Chemical Research of Catalonia (ICIQ), The Barcelona Institute of Science and Technology (BIST), Av. Paisos Catalans, 16,. Tarragona E-43007, Spain

[‡]Catalan Institute of Nanoscience and Nanotechnology (ICN2), CSIC and The Barcelona Institute of Science and Technology (BIST), Campus UAB, Bellaterra, 08193 Barcelona, Spain

[§]Catalonia Institute for Energy Research (IREC), Jardins de les Dones de Negre 1, Sant Adrià del Besòs, 08930 Barcelona, Catalonia, Spain

[∥]ICREA, Pg. Lluís Companys 23, 08010 Barcelona, Spain

Supporting Information

ABSTRACT: The development of upscalable oxygen evolving electrocatalysts from earth-abundant metals able to operate in neutral or acidic environments and low overpotentials remains a fundamental challenge for the realization of artificial photosynthesis. In this study, we report a highly active phase of heterobimetallic cyanide-bridged electrocatalysts able to promote water oxidation under neutral, basic (pH < 13), and acidic conditions (pH > 1). Cobalt−iron Prussian blue-type thin films, formed by chemical etching of $Co(OH)_{1.0}(CO_3)_{0.5}{\cdot}nH_2O$ nanocrystals, yield a dramatic enhancement of the catalytic performance toward oxygen production, when compared with previous reports for analogous materials. Electrochemical, spectroscopic, and structural studies confirm the excellent performance, stability, and corrosion resistance, even when compared with state-of-the-art metal oxide catalysts under moderate overpotentials and in a remarkably large pH range, including acid media where most cost-effective water oxidation catalysts are not useful. The origin of the superior electrocatalytic activity toward water oxidation appears to be in the optimized interfacial matching between catalyst and electrode surface obtained through this fabrication method.

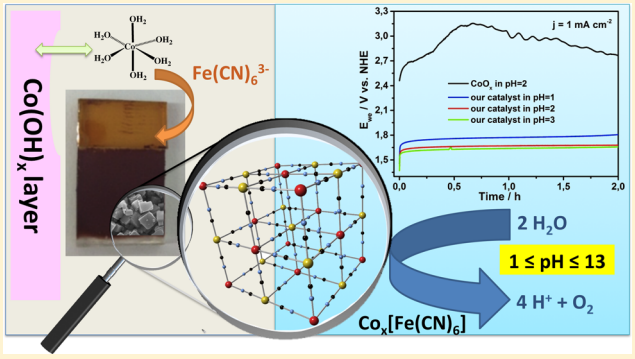

INTRODUCTION

The electrochemical oxygen evolution reaction (OER) is a very important anodic half-cell process in water splitting and CO_2 reduction applications.[1−3] Technologically relevant catalysts are needed for such applications to develop in the near future as a real alternative to the energy cycles, if economically viable.

Earth abundant electrocatalysts for OER in alkaline media have been extensively studied.[4−12] First row transition metal oxides of Co, Fe, or Ni (and their corresponding binary/ternary oxides) have extremely high activities but only at very high pH (pH > 13), where the corresponding half-cell reduction reaction (hydrogen production, for instance) is more difficult.[13] At lower pH, such catalysts suffer corrosion.[14] An efficient catalyst for OER at acidic[15−19] or near-neutral solution[20−24] based on earth abundant metals remains an important challenge and highly desirable for (photo)electrochemical devices, such as polymer electrolyte membrane (PEM) electrolyzers or artificial leaves. In such conditions, no catalyst has shown competitive performance compared with noble metals (Ir or Ru oxides), severely affecting the cost of this technology.

Several strategies to stabilize metal oxide catalysts in neutral or acidic media have been attempted.[25−28] The most remarkable was the discovery of a self-repairing process for the CoO_x OER catalysts in neutral media, as supported by the presence of excess phosphate anions in the electrolyte (Co−P_i).[12,21] Other attempts have included doping and nanostructuration.

Recently, several methods have been tested to control metal oxide corrosion in acid media to a certain extent. Manganese oxide catalysts can be useful although at very low potentials and currents;[18,19] or the corrosion process of intrinsically unstable metal oxides can be incorporated into the overall power to fuels scheme.[29] Unfortunately, these approaches do not match industry expectations in terms of current densities and energy efficiencies. Currently, only precious metal oxides match industrial requirements in neutral or acidic media, but this limits wide-applications owing to their scarcity and subsequent high cost.[30−32]

Received: September 18, 2016
Published: November 16, 2016

DOI: 10.1021/jacs.6b09778
J. Am. Chem. Soc. 2016, 138, 16037−16045

Accordingly, our own efforts in this area are focused on exploring for abundant metal-based active catalysts in neutral and acidic environments. In this line, we discovered that cobalt-containing Prussian blue-type analogues (PBAs) were promising water oxidation catalyst (WOC) materials.[33,34] PBAs are open metal−organic frameworks (MOF) with multiple applications due to their chemical versatility and stability.[35] PBAs have recently been investigated as an intriguing class of multifunctional materials in many energy-related fields, such as in supercapacitors,[36] lithium ion batteries,[37] microbial batteries,[38] sodium ion batteries,[39−41] self-rechargeable batteries, and so on.[42−44] Perfectly stabilized by the hexacyanoferrate group, cobalt hexacyanoferrates are robust and stable in a large pH range, including acidic and neutral conditions, exhibiting catalytic activities comparable to those of metal oxides for OER. Despite their robust performance, essential parameters such as current densities and mechanical resistance were still far from being competitive. We assigned these weaknesses to poor interfacial matching with electrode surfaces. In the study presented herein, we report a novel synthetic route for the preparation and processing of cobalt hexacyanoferrate (CoFe) WOC films, obtained via a template-assisted method. This alternative strategy has allowed us to reach rugged high current densities, from the excellent enhancement of the chemical, structural, and mechanical stability during the oxygen evolution reaction. This superior performance has also allowed us to corroborate the activity of CoFe films through detailed structural (pre- and postcatalysis) and electrochemical studies in a large pH range, including multiple surface sensitive techniques.

EXPERIMENTAL SECTION

Materials. All commercially available reagents and solvents were used as received without further purification unless otherwise indicated. Fluorine−tin−oxide coated glass slides (FTO, 12−14 Ω per square surface resistivity) were purchased from Pilkington NSG TEC 15A 2.2 mm slides with 80.0−81.5% transmittance. Nafion (5%) and all other chemical regents were purchased from Aldrich except $K_3Fe(CN)_6$ (98%, ACROS Organics) and KOH pellets (85%, Pan-Reac). If not specified, all solutions were prepared with Milli-Q water (ca. 18.2 MΩ·cm resistivity).

Electrode Preparation. FTO glass was cut into small pieces with 1 × 1.4 cm^2 area; a 1 × 1 cm^2 geometric surface area was created by masking one edge of the FTO plate with a wide stripe of Scotch tape. Prior to deposition, the glass slides were rinsed by sonication in soap, distilled water, and 2-propanol for 10 min.

CoO_x film. The CoO_x formula is used herein to indicate a cobalt oxo- or hydroxo-based solid that can incorporate additional countercations and anions (such as carbonate). CoO_x films were grown on FTO glass substrates via a hydrothermal process. Briefly, 77.5 mg $Co(NO_3)_2·6H_2O$ and 80.8 mg $CO(NH_2)_2$ powder were dissolved in 10 mL of Milli-Q water and then transferred into a 20 mL Teflon-lined autoclave with two pieces of FTO substrates immersed into the reaction solution (conductive side downward). The autoclave was maintained at 120 °C for 10 h and then cooled down to room temperature in air. After the reaction, the coated film on the nonconductive side was removed carefully using paper tissue. The FTO glass was rinsed with Milli-Q water several times. On the basis of structure and composition characterization, the formula of the product is $Co(OH)_{1.0}(CO_3)_{0.5}·nH_2O$.

CoFe Electrode. $K_3Fe(CN)_6$ powder (800 mg) was dissolved in 100 mL of Milli-Q water under vigorous stirring. One piece of CoO_x film was immersed in 9 mL of the freshly prepared $K_3Fe(CN)_6$ aqueous solution in a vial; after being left standing for 1 h, the glass vial was sealed and then heated at 60 °C for 3 h in the oven. During the reaction (Scheme 1), the color of the films changes initially from pink to brown. Subsequently, the vial was cooled down in air inside a fume hood.

Scheme 1. Schematic Representation of the Synthetic Procedure for the Transformation of the Metal Hydroxide into the More Stable Coordination Complex

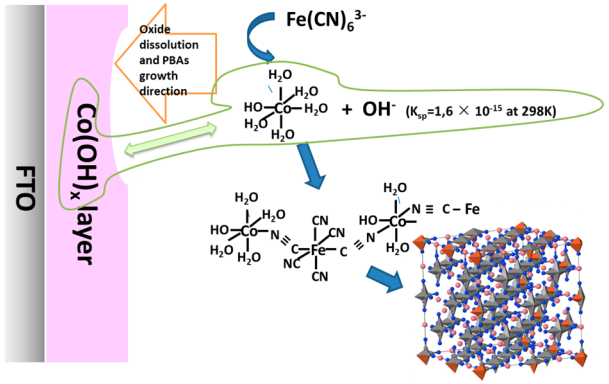

Finally, the CoFe electrode was gently rinsed with Milli-Q water to remove any impurities. The electrodes were left in the oven at 60 °C overnight. Prior to any electrochemical studies, all electrodes were immersed in 20 mL of concentrated H_2SO_4 solution (pH = 1) for at least 3 h to remove any remaining traces of CoO_x and then washed again with Milli-Q water. The average CoFe mass loading on the electrodes is 0.3 mg cm^{-2}.

CoFe(a) Electrode. In a typical synthesis, $Co(NO_3)_2·6H_2O$ (3.5 g) and $K_3[Fe(CN)_6]$ (1.75 g) were separately dissolved in formamide (100 mL each solution). Then, the $Co(NO_3)_2$ solution was poured on to the $K_3[Fe(CN)_6]$ solution at room temperature with vigorous stirring. The dark purple suspension was stirred for 2 h. The powder was isolated by centrifugation, rinsed with Milli-Q water, and finally dried at 60 °C. The CoFe(a) working electrode was obtained by drop-casting. A catalyst ink was prepared with Milli-Q water (100 μL), ethanol (340 μL), Nafion solution (5 wt %, 20 μL), and CoFe(a) (5 mg). The mixture was sonicated for 30 min to form a homogeneous suspension. Ink (27.6 μL) was then drop-cast by micropipette on a transparent FTO glass with a surface area of 1 × 1 cm^2. The solvent was evaporated at room temperature for about 20 min. The catalyst loading was 0.3 mg cm^{-2} or 1.05 mg cm^{-2} Nafion.

Scratched Electrode. CoFe solid was scratched from a CoFe electrode surface (0.3 mg). Then it was dispersed in a H_2O (25 μL)/ethanol (90 μL)/Nafion (5%, 5 μL) mixture. The resulting ink was sonicated for 30 min, and then spread by drop casting on a FTO glass with a surface area of 1 × 1 cm^2, following by drying at room temperature.

Electrochemical Methods. All electrochemical experiments were performed under ambient conditions with a Bio-Logic VMP3 multichannel potentiostat/galvanostat. The three-electrode configuration was completed with a saturated calomel electrode (SCE) reference electrode, and a Pt mesh counter electrode. All potentials are measured versus SCE and are reported versus the normal hydrogen electrode (NHE) using the equation of $E(NHE) = E(SCE) + 0.244$ V. Overpotentials were computed using $\eta = E(NHE) - 1.229 + 0.059$ pH. Ohmic drop was determined for all electrochemical data by using the automatic current interrupt (CI) method implemented with the potentiostat. In all cases, 0.1 M of phosphate buffer (KPi) solution at pH 7 was first prepared by dissolving appropriate amounts of K_2HPO_4 and KH_2PO_4 solid in 1 M KNO_3 solution. The pH was gradually increased or decreased by adding aliquots of concentrated KOH solution or concentrated H_3PO_4 in pH = 7 0.1 M KPi + 1 M KNO_3 solution while monitoring with pH meter. All cyclic voltammograms (CVs) were measured in a three-electrode one-compartment configuration with 50 mL of aqueous phosphate buffer solution. CVs were run at a scan rate of 5 mV s^{-1} unless otherwise noted. Chronopotentiometric measurements (CPs) were recorded at a constant current density as a function of pH in a fritted H-shaped cell under vigorous stirring. The platinum mesh electrode was inserted into one compartment (cathodic reaction), while the modified working

DOI: 10.1021/jacs.6b09778
J. Am. Chem. Soc. 2016, 138, 16037−16045

electrode and a reference electrode were inserted in the anodic compartment. Steady-state current densities for Tafel analyses were collected at a variety of applied potentials during oxygen evolution at different pH. Working potential was swept from low to high values with 50 mV increments across the linear Tafel region. At each potential, the current was stabilized for 10 min to attain a steady-state value with the stirred solution (600 rpm). The oxygen evolution efficiencies were determined from the total amount of charge Q (C) passed through the cell. Assuming that four electrons are needed to produce one O_2 molecule, the theoretical yield can be calculated as follows:

$$nO_2 = \frac{Q}{4F}$$

where F is the Faraday constant. The total mole of oxygen produced was quantitatively determined by using a calibrated Ocean Optics FOXY probe.

Potentiostatic Electrochemical Impedance Spectroscopy (PEIS). PEIS measurements were conducted with a Bio-Logic VMP3 multichannel potentiostat/galvanostat equipped with a built-in electrochemical impedance spectroscopy (EIS) analyzer at pH 7. The CoFe and scratched electrode were assessed in the OER potential range with an initial conditioning for 1 min. The amplitude of the sinusoidal wave was 5 mV. The frequency scan range was 100 kHz to 0.01 Hz. The fitting was calculated on the basis of a Randles equivalent circuit model (shown in Scheme S1) employing constant phase.

Characterization Methods. Scanning electron microscopy (SEM) micrographs were acquired on an FEI Quanta 650 FEG ESEM, 20 kV, equipped with an Oxford EDX analyzer (Oxford Instruments). Five nanometers of Pt was deposited onto the as-prepared CoFe samples for SEM checking by using magnetron sputtering LEICA EM ACE600. The chemical composition and the structure of the products were characterized by powder X-ray diffraction (XRD; Bruker Kappa APEX II DUO diffractometer equipped with an APPEX 2 4K CCD area detector). Infrared transmittance spectra (Alpha Bruker FTIR equipped with attenuated total reflectance sample holder) and Raman spectroscopy (Renishaw in Via Reflex Raman confocal microscope, Gloucestershire, U.K., light source 514 nm). The TEM specimens were prepared by scratching as-prepared CoFe powders from the FTO substrate, followed by dispersing them in cyclohexane and collecting them on the TEM copper grids. High-resolution transmission electron microscopy (HRTEM) images and scanning transmission electron microscopy (STEM) studies were conducted by using an FEI Tecnai F20 field emission gun microscope operated at 200 kV with a point-to-point resolution of 0.19 nm, which is equipped with high angle annular dark field (HAADF) and electron energy loss spectroscopy (EELS) detectors.[45−47]

RESULTS AND DISCUSSION

Synthesis and Structural Characterization. Because of its easy processability and well-studied dissolution behavior, cobalt hydroxide was chosen as metal reservoir. In a typical synthetic procedure (Scheme 1), a thin pink film of CoO_x was initially grown on a transparent fluoride-doped tin oxide (FTO) surface by a hydrothermal method. The CoO_x formula is used herein to indicate a cobalt oxo- or hydroxo-based solid that can incorporate additional counter-cations and anions (such as carbonate). Characterization by field-emission scanning electron microscopy (FESEM) showed that CoO_x films are composed of nanowires of around 100 nm diameter and 7−8 μm length (Figures 1a and S1). Next, CoO_x films were used as a sacrificial template by immersion in an aqueous solution containing potassium hexacyanoferrate. The reaction was promoted by mild heating at 60 °C. Local dissolution of the metal oxide in neutral or slightly acidic media provides aqua cobalt ions, which were immediately consumed by excess ferricyanide ions to form a CoFe framework at the CoO_x/solution interface (Figure 1).

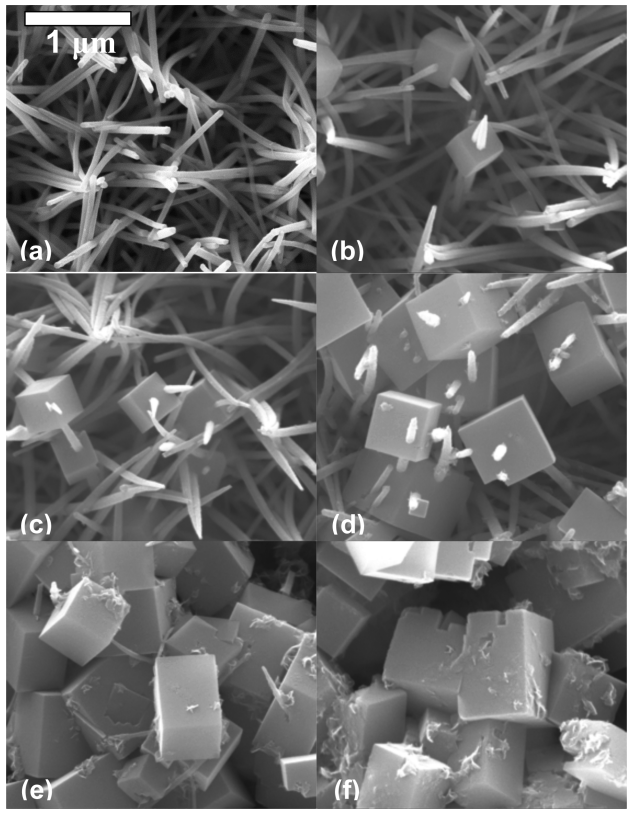

Figure 1. FESEM images of CoO_x (a) and of the transformation into a CoFe Prussian blue film by chemical etching with potassium hexacyanoferrate after 0.5 (b), 1 (c), 1.5 (d), 2 (e), and 3 h (f).

During the reaction, the sample color gradually changed from pink to brown (Figure S2). FESEM images taken at different times showed how the CoO_x wires acted as nucleation sites, with well-formed cubic-shaped crystals growing out of them. After 3 h, the wire network was completely substituted by a compact macroporous layer of cubic crystallites in the 50 nm to 1 μm range. Finally, the CoFe functionalized electrode was immersed in 20 mL of H_2SO_4 solution (pH = 1) for at least 3 h to completely remove any remaining traces of the CoO_x precursor (Figure S3). Composition and structural characterization by IR and Raman spectra and XRD pattern confirmed the purity of the final CoFe product. No sign of CoO_x could be detected (Figures S4−S6).

We used K-edges for O, C, and N and L edges for Co and Fe maps during the EELS studies. The annular dark field STEM (ADF STEM) micrograph in Figure S7 reveals the nanocube structure of a CoFe sample and the EELS chemical composition maps obtained from the indigo squared area in the ADF STEM micrograph. As observed in these maps, C, N, Fe, and Co elements were homogeneously distributed throughout the nanocube structures, supporting the presence of CoFe Prussian blue.

Direct TEM analysis of local atomic structure has proven to be critical for understanding the relationship between lattice microstructure and microscopic behavior.[48] However, the coordination polymers are especially susceptible to electron beam damage, even at very short exposure times, which makes it difficult to reach stable atomic-level TEM observation of Fe and Co atom arrays within the CoFe lattice. Itoi et al. have succeeded in exploring ionic liquids to stabilize CoFe PB nanoparticles for electron microscopy for the first time and give

DOI: 10.1021/jacs.6b09778
J. Am. Chem. Soc. 2016, 138, 16037−16045

spatial information on the local microstructure at the atomic level.[49] In our case, after 15 min electron beam shower at 200 kV to remove possible organic impurities and water molecules at room temperature, clear TEM images can still be easily obtained without degradation, and the fringes associated with the cubic structure are clearly observed. Figure 2 and

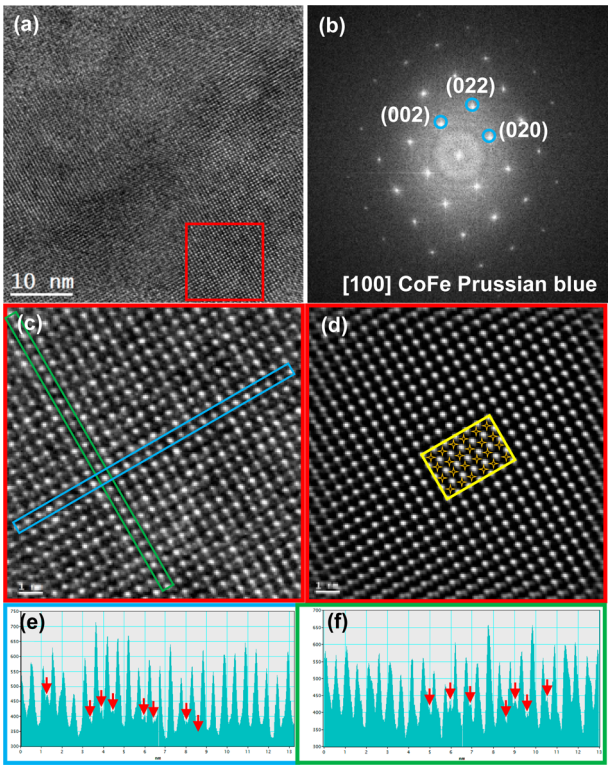

Figure 2. (a) HRTEM micrograph of as-prepared CoFe showing a general view of a nanocube structure. (b) Corresponding power spectrum indicating cubic [$Fm\bar{3}m$]-space group, with lattice parameters a = 1.02794, b = 1.02794, and c = 1.02794 nm, as visualized along the [100] direction. (c) Atomic resolution TEM image of the red rectangle area in panel a. (d) Periodic structure extracted by inverse Fourier filtering. Yellow rectangle area inset shows Co and Fe atomic positions. Dark spots marked with orange stars are the centers of the Co−Fe cubic lattices. Bright spots correspond to the Wyckoff site 8 of the $Fm3m$ space group. (e,f) TEM intensity profile along the (002) and (020) planes, respectively, corresponding to the indigo and green regions in panel c.

Figure S8 display HRTEM images and a general power spectrum image of as-prepared CoFe at room temperature. A coherent shepherd-check pattern is related to the alternating Co atom and Fe atom arrays. We measured the mean Co−Fe distance to be about 5.15 Å, which is consistent with the value determined by X-ray diffraction in crystalline samples (5.15 Å) corresponding to the half-cell parameter a = 10.3 Å determined by PXRD. The bottom images in Figure 2 show the TEM intensity profiles obtained along as-prepared (002) and (020) planes. The inhomogeneous peak densities further demonstrate the presence of vacancies, as expected in these nonstoichiometric compounds. We compared the simulated HRTEM, temperature colored HRTEM images, and power spectrum of different PBA-1, PBA-2, PBA-3, and PBA-4 models (Figure S9A−D) with that of the experimental sample, to identify our CoFe phase as $Co_4(Fe(CN)_6)_{2.67}(H_2O)_{15.33}$-[$Fm\bar{3}m$]-225 (PBA-4, Figure S10).

Electrocatalysis. The water oxidation catalytic activity of as-prepared CoFe was first appraised via CVs in neutral aqueous solution buffered at pH = 7 using a 0.1 M phosphate solution containing 1 M KNO_3 as supporting electrolyte. As shown in Figure 3a, at more positive potentials a pronounced

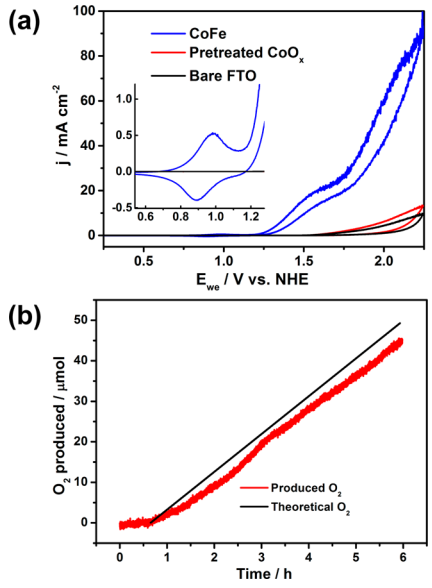

Figure 3. (a) Cyclic votammograms of CoFe (blue curve), CoO_x after acid pretreatment (red curve), and bare FTO (black curve). Inset is enlarged region [0.6−1.3 V]. Conditions are as follows: 50 mL of 0.1 M PKi + 1 M KNO_3 phosphate buffer, pH = 7, scan rate 5 mV s^{-1}. (b) O_2 amounts monitored by fluorescence-quench probe (red trace) and theoretical O_2 calculated assuming 100% Faradaic efficiency (black trace). Conditions: 0.1 M PKi + 1 M KNO_3 buffer, pH = 7, j = 1 mA cm^{-2}.

catalytic wave appeared with a sharp onset at 1.15 V vs NHE (334 mV overpotential). During the oxidative process (in the positive direction), a substantial amount of oxygen bubbles were observed (seen in the Supporting Information Video). In the inset, there is a small reversible redox couple at an equilibrium potential of 0.94 V (= [0.89 V + 0.98 V]/2), which can be assigned to the Co^{II}/Co^{III} redox process. Once the catalytic event starts, there is a change in slope above 1.5 V that we assign to mass-transport limitations to OER. This plateau disappears above 1.8 V. This reactivation of the electrocatalytic process at high potentials could also be related to a change in the redox state of the PBA, into a Co^{III}/Fe^{III} phase, that might be more active. *In operando* experiments would be useful to determine the origin of this feature.

We monitored the evolved oxygen from a CoFe catalyst film by a florescence O_2 sensor in a gastight cell during sustained electrolysis at a constant current density in neutral (pH 7) and acidic (pH 2) media (red line in Figure 3b and Figure S11), respectively. The theoretical oxygen yield was calculated from the total charge passed during electrolysis (black line). Efficiencies above 92% were found, indicating that the catalytic current density is mainly originating from the water oxidation process.

The catalytic stability was evaluated by tracking the applied potential over time using galvanostatic measurements at constant current density of 1 mA cm^{-2} in pH 7 KPi + 1 M KNO_3 electrolyte (Figure 4a). CoFe electrodes have an excellent stability. After 30 min induction time, the potential remains constant over 8 h, without any sign of degradation. In order to

DOI: 10.1021/jacs.6b09778
J. Am. Chem. Soc. 2016, 138, 16037−16045

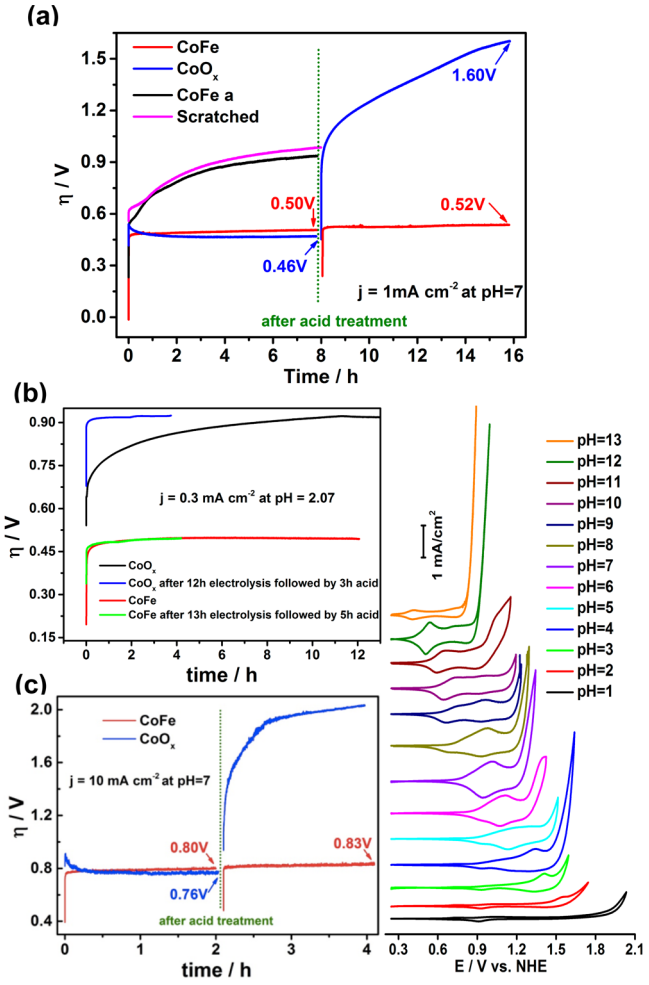

Figure 4. (a) Overpotential versus time data, under a constant current density of 1 mA cm^{-2} in pH 7 phosphate buffer, of as-synthesized CoFe catalyst (red curve), CoFe(a) (black curve), and scratched (magenta curve) and one original CoO_x (blue curve), which was directly used after hydrothermal preparation without any acid pretreatment, respectively. (b) Electrochemical stability by sustained chronamperometry at 0.3 mA cm^{-2} for as-prepared CoFe and one original CoO_x electrode in 0.1 M KPi + 1 M KNO_3 buffer at pH 2. Following that, both electrodes were soaked in pH 1 H_2SO_4 solution for several hours and then were re-examined again under the same conditions. (c) Analogous comparative chronoamperometry in pH 7 phosphate buffer, of as-synthesized CoFe catalyst (red curve) and one original CoO_x (blue curve) under a constant current density of 10 mA cm^{-2}. (d) Representative CVs of as-prepared CoFe electrode at a scan rate of 5 mV s^{-1} in 0.1 M KPi + 1 M KNO_3 solution at various pH values.

investigate the effect of pH on the electrochemical stability of CoFe, we carried out bulk water electrolysis as a function of pH. CoFe remains both chemically and electrochemically stable (Figures 4b and S12−S15), not showing any significant changes in performance with time in the 2 ≤ pH ≤ 13 range. At pH 1, catalytic activity decreases substantially. Significantly higher overpotentials are needed to maintain the desired current density. Additionally, durability is also an issue, and activity apparently decreases with time. However, it is worth mentioning that CoFe is not intrinsically unstable in strong acid. For instance, this was confirmed by placing a CoFe electrode in pH = 1 H_2SO_4 solution for 13 h without bias, after performing water electrolysis at pH 12. The chronopotentiometry experiments confirm identical electrocatalytic activity before and after the acid treatment (Figure S13). At pH 14, CoFe is unstable and decomposes, probably to an oxo/hydroxo derivative (Figure S16).

We also carried out stability tests at moderate current densities (10 mA cm^{-2}), following the benchmarking protocol proposed by Jaramillo et al. (Figure 4c and S17).[10] In these conditions, we also observed good stability for the CoFe electrodes. At neutral pH, the stability and activity are comparable to that of CoO_x, but again the CoFe electrode maintains its performance after washing the electrode with concentrated sulfuric acid. Remarkably, the CoFe electrodes maintain stable current densities down to pH = 2. It is worth mentioning that the overpotential to reach 10 mA cm^{-2} at this pH is the lowest when compared with higher pH conditions.

CVs of CoFe were collected in the 1 < pH < 13 range (Figure 4d). The appearance of the water oxidation wave, as expected, is significantly pH dependent. The reversible Co^{II}/Co^{III} redox couple also shows pH dependence that could be related to electronic changes at the water coordinated Co sites, due to the higher proton concentration (Figure S18). At high pH, the redox wave splits in two reversible processes. This could be related to different protonation of water molecules bound to active sites at intermediate hydroxyl concentrations.

The Tafel behavior of the catalyst in the region of water oxidation was measured over a wide pH range spanning acidic, neutral, and alkaline conditions (Figure 5a), and its linear

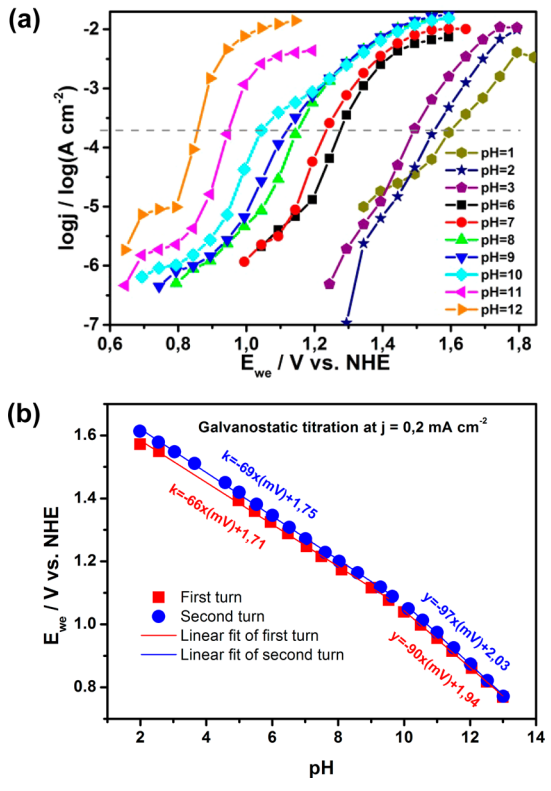

Figure 5. (a) The plots of log j with respect to E (vs NHE) for as-prepared CoFe operated in 0.1 M KPi + 1 M KNO_3 buffer solution over a wide pH region, going from right to left, from pH 1 to 12. A straightforward horizontal slice through 0.2 mA cm^{-2} is marked by gray dotted line. (b) Potential dependence of our catalyst on pH at constant current density of 0.2 mA cm^{-2} operated in phosphate buffer solution. First data set (■), which was collected on a freshly prepared electrode, is compared with a subsequent data set (●) using the same electrode.

DOI: 10.1021/jacs.6b09778
J. Am. Chem. Soc. 2016, 138, 16037−16045

region is shown in Figure S19. Close inspection revealed that the Tafel slopes generally decreased from low to high pH. Specifically, at alkaline pH 10−12, the Tafel slopes are near the theoretical value of 59 mV/decade that corresponds to 2.3 RT/F. This slope is characteristic of an oxygen evolution mechanism involving a reversible one-electron transfer prior to a chemical turnover-limiting process.[18,24] At pH 9, the Tafel slope changes. This change suggests a different rate-determining step during water oxidation below this pH value.

We conducted galvanostatic titration to get additional information about the pH dependence of water oxidation. The required potential to sustain a constant current density of 0.2 mA cm^{-2} was measured in the pH = 2−13 range (Figure 5b). The applied potential increases monotonically with pH value up to pH 9. After that, a significant change in the pH-dependent behavior is observed. The low pH slope of 66 mV/pH changes to 90 mV/pH above pH 10, which is in accordance with the result from Tafel analysis (Figure S20), indicates a change in mechanism. Both slopes are reproducible and consistent among independent and the sequential runs.

Control Experiments and Postcatalysis Characterization. For water oxidation catalysts, the question about the true species is usually raised. The *in situ* formation of metal oxide (CoO_x) needs to be precluded. During our electrocatalysis experiments, CoO_x could be produced in two possible ways: as remains of the starting material or from CoFe decomposition in the harsh oxidizing environment. Therefore, we gathered enough electrochemical, XRD, IR, Raman, HRTEM, and EELS mapping to provide clear evidence of the genuine WOC activity of the CoFe component. In addition, we carried out multiple control experiments.

For instance, we compared a chronopotentiometry (CP) experiment at 1 mA cm^{-2} between precursor material CoO_x and CoFe in neutral pH (Figure 4a). Both species give a similar and consistent overpotential. After 8 h, both electrodes were immersed in fresh 60 mL of H_2SO_4 solution (pH 1) overnight, under open-circuit conditions. During this process, the CoO_x electrode completely turned into a transparent film within 20 min (Figure S21). When a second CP was attempted at neutral pH, the overpotential kept increasing with time due to the corrosion of the CoO_x catalyst. In contrast, the CoFe electrode was not affected by the acid treatment, and a consistent overpotential was maintained during a second run, without any appearance of fatigue.

The comparison of OER activity in acidic media is even more significant. One piece of original precursor CoO_x electrode proved to be highly unstable over the course of electrolysis at pH 2 (Figures 4b and S12). The oxygen gas evolution in this case is accompanied by significant dissolution of the oxide film during sustained electrolysis under acidic conditions.

The morphology, composition, and structure stability of the CoFe films was also confirmed by multiple analyses before and after intense oxygen evolution. Microscopic graphics clearly showed no obvious aggregation among CoFe nanoparticles (Figure S22) and no changes in Fe/Co ratio (Figure S23), and no O signal was detected in element mapping, as expected from oxide formation (Figure 6). There is no significant difference between the as-used and the as-prepared CoFe, in either position or shape of peaks, discarding any crystallinity loss or any decrease in particle size from Raman and IR spectra, PXRD data, and HRTEM micrographs (Figure S24 and S25), which support the preservation of crystal structure and composition after long-term bulk electrolysis.

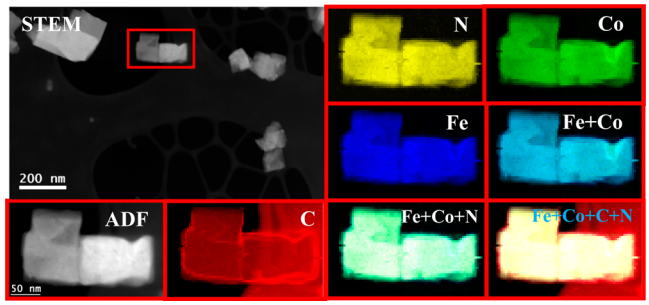

Figure 6. EELS chemical composition maps obtained from the red rectangle area of the STEM-ADF micrograph. Individual C (red), N (yellow), Co (green), and Fe (blue) maps and their composites. The extra C signal at the right side of the mapping image is derived from the holey carbon grid.

Enhanced Electrocatalytic Activity. To further investigate the benefits of our novel processing method, we quantitatively compared the present CoFe films with those obtained by preparation methods previously reported, noted CoFe(a) (details of electrode preparation are provided in the Experimental Section). All electrodes show comparable current densities in OER region at lower overpotentials. Remarkably, only our CoFe electrode, as obtained from the etching process, keeps the electrocatalytic activity at high overpotentials (high current densities). The low performance at high overpotentials for the CoFe(a) films was attributed to mechanical instability, being easily detached from the FTO surface because of gas evolution (Figure S26).

Interestingly, if we scratch the catalytic film from one of our as-prepared CoFe samples, this powder does not exhibit better electrocatalytic performance when compared with CoFe(a). All CoFe-derivatives exhibit consistent and analogous activity when processed as Nafion/EtOH/H_2O inks on FTO for the same catalysts loadings (details of the electrode preparation are provided in the Experimental Section). This supports the crucial role of the CoFe−FTO interface as constructed from our novel preparation process (Figure S27).

PEIS in 0.1 M KP_i + 1 M KNO_3 aqueous solution at pH 7 under different anodic potentials is recorded, and its representative results are shown in Figures S28 and S29. A frequency window between 100 kHz and 0.01 Hz was chosen. The electronic elements responded differently in the various frequency regions. For example, the movement of ions in electrolyte and electrons on conductive material is a fast process and has very quick response speed when an AC voltage is applied, so its corresponding element appears in the high frequency range of EIS spectra. Electrochemical reactions on the electrode surface is considered to take a longer time to occur and thus the capacitive semicircle at moderate and low frequencies is typical for charge transfer (R_{ct}) controlled kinetics. The characteristic time constant of the charge transfer processes decrease with increasing overpotential.

We performed comparative experimental impedance studies for scratched and CoFe films for insight into the origin of the difference in catalytic activity to OER. As shown in Tables S2 and S3, the resistance, R_f, is the same for CoFe and scratched anodes (around 146 Ω cm^{-2}) and remains potential independent, which means the contribution from (R_fQ_f) component is identical. The variation of R_{ct}, Q_{dl}, and τ ($R_{ct}Q_{dl}$) with electrode potentials was recorded for further comparison. $R_{ct}Q_{dl}$ is the time constant of the faradic reaction and can be considered

DOI: 10.1021/jacs.6b09778
J. Am. Chem. Soc. 2016, 138, 16037−16045

as a proper parameter to characterize the intrinsic catalytic activity of catalyst.[50] The lower value means faster kinetics of the reaction.[51,52] It can be seen that the RC time constant of this loop lies in the measurement window from 100 kHz to 0.01 Hz and decreases as the potential is increased from 1.174 to 1.344 V vs NHE, reflecting the increasing rate of electron transfer in the OER process. Because CoFe powders and its loading (0.3 mg cm^{-2}) are the same for CoFe and scratched electrode, their intrinsic catalytic activities should be identical, which is apparently consistent with the experimental results shown in Figure 7c. Note that the intrinsic catalytic activity for

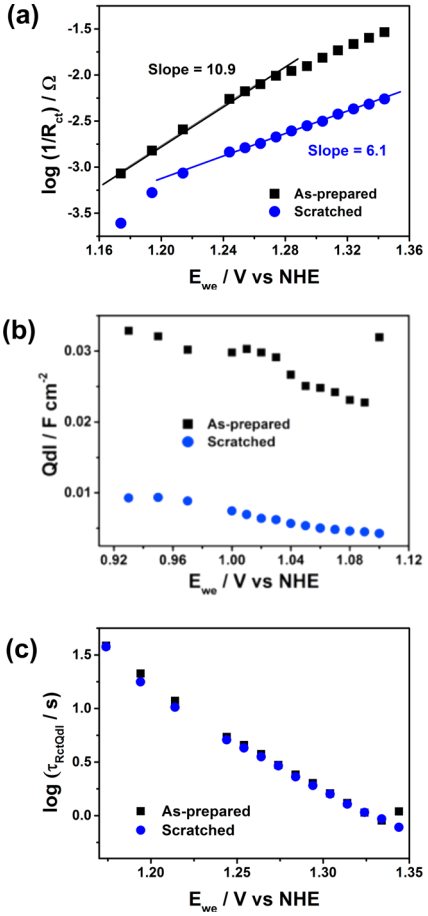

Figure 7. Comparative EIS data representing the potential dependence of the charge transfer R_{ct} (a), double layer capacitance Q_{dl} (b), and time constant $R_{ct}Q_{dl}$ (c) for CoFe and scratched electrodes. These values were summarized in Tables S2 and S3 as derived from the fitting to an equivalent circuit as shown in Scheme S1.

OER (assessed by time constant $R_{ct}Q_{dl}$) is different from the overall catalytic activity (assessed by R_{ct}). For CoFe electrode, from 1.18 to 1.28 V, the resistance, R_{ct}, to charge transfer process decreases with a Tafel slope of 91 mV dec^{-1} (the reciprocal of 10.9), which is calculated according to the following derivative:[53,54]

$$\log\left(\frac{1}{R_{ct}}\right) = \log\left(\frac{di}{d\eta}\right) = \frac{1}{b}\eta + \log\left(\frac{2.3i_0}{b}\right)$$

For both electrodes, the observed slight decrease of Q_{dl} with increasing potential can also be related to the decrease of the available outer surface area of the electrode due to the sticking of gas bubbles. Compared to CoFe film, the smaller Q_{dl} value for the scratched electrode suggests less accessible active surface area due to the "dead volume" throughout the whole film caused by drop coating, indicating that a large fraction of the catalyst surface was not fully utilized; in other words, the strategy used to prepare CoFe via template-assisted method is a more effective way to obtain an electrode with higher active surface area.

DISCUSSION

The benefits of the chemical etching method upon CoFe performance cannot be due to a different reaction mechanism, as confirmed from electrochemical data. Tafel slope and EIS data are undistinguishable. Additionally, once detached from the original FTO substrate, performance is also comparable to CoFe(a). The faster kinetics yielding higher current densities must be related to superior electron or mass transport in the as-prepared crystallites originally attached to the substrate as grown from the CoO_x starting material. We have identified several differences that can be at the origin of these observations:

(1) The new processing method yields significantly higher density of electroactive sites. The surface coverage estimated from the cyclic voltagrammograms (Figure S30 and eq S1) indicate a density of active sites of 110 nmol/cm^2 in CoFe, when only 32 nmol/cm^2 active sites were found for CoFe(a).

(2) The connection of the crystallites to the FTO support is stronger, mechanically and electronically. This connectivity may take advantage of the initial matching between FTO and CoO_x, both oxide compounds. This offers faster electron transfer toward the catalytic sites and excellent mechanical stability. This is illustrated by the excellent stability of the CoFe electrodes when compared with those previously reported. Sustained current densities over 10 mA cm^{-2} can be reached in the present case, whereas 0.5 mA cm^{-2} was the experimental limiting current in the previous case.[33]

(3) In the same line, the CoO_x nanowire template for the CoFe nuclei growth avoids crystallite agglomeration and a densely packed film, contrary to the case when using electrodeposition or drop coating methods. Thus, all crystallites formed are well connected to the FTO support and to one another, as grown following the wired network (Figure 1).

(4) The final stoichiometry achieved in this case is also different. A 1.5 Co/Fe ratio is found in the CoFe electrodes, when 1.1 was found in ref 33. This also contributes to the higher active site density.

On the possible reaction mechanism below pH = 9, shared by all PBAs, we propose a single site pathway. A concerted mechanism is not feasible in this case, although it is preferred for most heterogeneous catalysts, including CoO_x.[55] The closest Co···Co distance (7.7 Å) in the PBA unit cell does not allow for direct transfer of a water molecule between neighboring metal centers, or for the formation of bridging peroxide intermediates. We do not assign any catalytic activity to the Fe centers, since they are coordinatively saturated by six cyanide ligands. Its function is structural (giving solid-state stability) and electronic (promoting electron transfer).

Given the stoichiometry in the CoFe electrodes ($Co_4Fe_{2.67}$), each Co center has two coordinated water molecules on average. To determine if the presence of these two water molecules in

DOI: 10.1021/jacs.6b09778
J. Am. Chem. Soc. 2016, 138, 16037−16045

cis coordination is important for the catalytic cycle, we carried out poisoning tests by adding an excess of 2,2′-bipyridyl (bpy). This chelating ligand is selective for *cis* configuration when substituting water molecules. We determined that electrochemical data is not affected by the presence of bpy (Figure S31), what suggests that *cis* conformation is not a key issue for catalysis. From all these observations, our proposed single-site mechanism follows the well-established route of four concerted one e^-/one H^+ transfer events, as established for several homogeneous catalysts.[56,57] The O−O bond formation should occur through nucleophilic attack of a water molecule (noncoordinated) to the electrodeficient oxo/oxyl species generated upon two successive oxidations (Figure S32). As discussed before, *in operando* experiments will be needed to detect these intermediates to support this hypothesis.

CONCLUSIONS

In summary, we are disclosing a novel processing for the preparation of electrocatalytic Co−Fe Prussian blue-type films taking advantage of a chemical etching process. This preparation allows solutions for many of the problems found in these water oxidation catalysts, such as low currents and poor mechanical (short-term) stability. These new films promote orders of magnitude higher electrocatalytic currents than previously reported and excellent long and short-term stability, even at current densities over 10 mA cm^{-2}. Furthermore, the latter has allowed us to perform detailed studies in a large pH range. Our pH-dependent data confirms the unique versatility of these PB-type water oxidation catalysts, able to promote oxygen evolution in a large pH range (1 < pH < 13) unparalleled by any other WOC ever reported. Particularly remarkable is their stability to acid, along with the fact that the lower overpotentials were found at pH = 2. Structure and activity persist even in concentrated sulfuric acid. These CoFe materials represent the first heterogeneous non-noble metal WOCs, active and corrosion resistant in acid media, where hydrogen production is preferred in a water splitting platform.

ASSOCIATED CONTENT

Supporting Information

The Supporting Information is available free of charge on the ACS Publications website at DOI: 10.1021/jacs.6b09778.

Additional electrochemical data, composition and structural characterization by IR and Raman, XRD, SEM and TEM, and proposed mechanistic pathway (PDF)

Video showing oxygen bubbles formed during oxidative process (MPG)

AUTHOR INFORMATION

Corresponding Author

*jrgalan@iciq.es

ORCID

Jordi Arbiol: 0000-0002-0695-1726

Jose Ramon Galan-Mascaros: 0000-0001-7983-9762

Notes

The authors declare no competing financial interest.

ACKNOWLEDGMENTS

This work was supported by the European Union (Project ERC StG Grant CHEMCOMP No. 279313); the Spanish Ministerio de Economía y Competitividad (MINECO) through Projects CTQ2015-71287-R, TNT-FUELS, and e-TNT (MAT2014-59961-C2-2-R) and the Severo Ochoa Excellence Accreditations 2014−2018, SEV-2013-0319 and SEV-2013-0295, the Generalitat de Catalunya (2014-SGR-797 and 2014-SGR-1638), and the ICIQ foundation. A.R.C. thanks the Marie Curie COFUND Action from the European Commission for cofinancing his postdoctoral fellowship. L.H. thanks MINECO for her predoctoral fellowship. The research leading to these results has also received funding from "La Caixa" Foundation. Part of the present work has been performed in the framework of Universitat Autònoma de Barcelona Materials Science Ph.D. program.

REFERENCES

(1) McEvoy, J. P.; Brudvig, G. W. *Chem. Rev.* **2006**, *106*, 4455.

(2) Blakemore, J. D.; Crabtree, R. H.; Brudvig, G. W. *Chem. Rev.* **2015**, *115*, 12974.

(3) Yagi, M.; Kaneko, M. *Chem. Rev.* **2001**, *101*, 21.

(4) Chen, S.; Qiao, S.-Z. *ACS Nano* **2013**, *7*, 10190.

(5) Moir, J.; Soheilnia, N.; O'Brien, P.; Jelle, A.; Grozea, C. M.; Faulkner, D.; Helander, M. G.; Ozin, G. A. *ACS Nano* **2013**, *7*, 4261.

(6) Luo, J.; Im, J.-H.; Mayer, M. T.; Schreier, M.; Nazeeruddin, M. K.; Park, N.-G.; Tilley, S. D.; Fan, H. J.; Grätzel, M. *Science* **2014**, *345*, 1593.

(7) Smith, R. D. L.; Prévot, M. S.; Fagan, R. D.; Zhang, Z.; Sedach, P. A.; Siu, M. K. J.; Trudel, S.; Berlinguette, C. P. *Science* **2013**, *340*, 60.

(8) Niu, K. Y.; Lin, F.; Jung, S.; Fang, L.; Nordlund, D.; McCrory, C. C.; Weng, T. C.; Ercius, P.; Doeff, M. M.; Zheng, H. *Nano Lett.* **2015**, *15*, 2498.

(9) Liang, H.; Meng, F.; Caban-Acevedo, M.; Li, L.; Forticaux, A.; Xiu, L.; Wang, Z.; Jin, S. *Nano Lett.* **2015**, *15*, 1421.

(10) McCrory, C. C.; Jung, S.; Peters, J. C.; Jaramillo, T. F. *J. Am. Chem. Soc.* **2013**, *135*, 16977.

(11) Zhang, B.; Zheng, X.; Voznyy, O.; Comin, R.; Bajdich, M.; García-Melchor, M.; Han, L.; Xu, J.; Liu, M.; Zheng, L.; García de Arquer, F. P.; Dinh, C. T.; Fan, F.; Yuan, M.; Yassitepe, E.; Chen, N.; Regier, T.; Liu, P.; Li, Y.; De Luna, P.; Janmohamed, A.; Xin, H. L.; Yang, H.; Vojvodic, A.; Sargent, E. H. *Science* **2016**, *352*, 333.

(12) Lutterman, D. A.; Surendranath, Y.; Nocera, D. G. *J. Am. Chem. Soc.* **2009**, *131*, 3838.

(13) Subbaraman, R.; Tripkovic, D.; Strmcnik, D.; Chang, K.-C.; Uchimura, M.; Paulikas, A. P.; Stamenkovic, V.; Markovic, N. M. *Science* **2011**, *334*, 1256.

(14) McCrory, C. C.; Jung, S.; Ferrer, I. M.; Chatman, S. M.; Peters, J. C.; Jaramillo, T. F. *J. Am. Chem. Soc.* **2015**, *137*, 4347.

(15) Wu, J.; Liu, M.; Chatterjee, K.; Hackenberg, K. P.; Shen, J.; Zou, X.; Yan, Y.; Gu, J.; Yang, Y.; Lou, J.; Ajayan, P. M. *Adv. Mater. Interfaces* **2016**, *3*, 1500669.

(16) Pokhrel, R.; Goetz, M. K.; Shaner, S. E.; Wu, X.; Stahl, S. S. *J. Am. Chem. Soc.* **2015**, *137*, 8384.

(17) Frydendal, R.; Paoli, E. A.; Chorkendorff, I.; Rossmeisl, J.; Stephens, I. E. L. *Adv. Energy Mater.* **2015**, *5*, 1500991.

(18) Huynh, M.; Bediako, D. K.; Nocera, D. G. *J. Am. Chem. Soc.* **2014**, *136*, 6002.

(19) Huynh, M.; Shi, C.; Billinge, S. J.; Nocera, D. G. *J. Am. Chem. Soc.* **2015**, *137*, 14887.

(20) Jin, K.; Chu, A.; Park, J.; Jeong, D.; Jerng, S. E.; Sim, U.; Jeong, H.-Y.; Lee, C. W.; Park, Y.-S.; Yang, K. D.; Kumar Pradhan, G.; Kim, D.; Sung, N.-E.; Hee Kim, S.; Nam, K. T. *Sci. Rep.* **2015**, *5*, 10279.

(21) Kanan, M. W.; Nocera, D. G. *Science* **2008**, *321*, 1072.

(22) Zaharieva, I.; Chernev, P.; Risch, M.; Klingan, K.; Kohlhoff, M.; Fischer, A.; Dau, H. *Energy Environ. Sci.* **2012**, *5*, 7081.

(23) Dogutan, D. K.; McGuire, R., Jr.; Nocera, D. G. *J. Am. Chem. Soc.* **2011**, *133*, 9178.

(24) Surendranath, Y.; Kanan, M. W.; Nocera, D. G. *J. Am. Chem. Soc.* **2010**, *132*, 16501.

(25) Young, E. R.; Nocera, D. G.; Bulović, V. *Energy Environ. Sci.* **2010**, *3*, 1726.

DOI: 10.1021/jacs.6b09778
J. Am. Chem. Soc. 2016, 138, 16037−16045

(26) Kim, H.; Park, J.; Park, I.; Jin, K.; Jerng, S. E.; Kim, S. H.; Nam, K. T.; Kang, K. *Nat. Commun.* **2015**, *6*, 8253.
(27) Tae, E. L.; Song, J.; Lee, A. R.; Kim, C. H.; Yoon, S.; Hwang, I. C.; Kim, M. G.; Yoon, K. B. *ACS Catal.* **2015**, *5*, 5525.
(28) Cobo, S.; Heidkamp, J.; Jacques, P. A.; Fize, J.; Fourmond, V.; Guetaz, L.; Jousselme, B.; Ivanova, V.; Dau, H.; Palacin, S.; Fontecave, M.; Artero, V. *Nat. Mater.* **2012**, *11*, 802.
(29) Bloor, L. G.; Molina, P. I.; Symes, M. D.; Cronin, L. *J. Am. Chem. Soc.* **2014**, *136*, 3304.
(30) Xu, J.; Aili, D.; Li, Q.; Christensen, E.; Jensen, J. O.; Zhang, W.; Hansen, M. K.; Liu, G.; Wang, X.; Bjerrum, N. J. *Energy Environ. Sci.* **2014**, *7*, 820.
(31) Jones, R. J.; Shinde, A.; Guevarra, D.; Xiang, C.; Haber, J. A.; Jin, J.; Gregoire, J. M. *ACS Comb. Sci.* **2015**, *17*, 71.
(32) Grigoriev, S. A.; Porembsky, V. I.; Fateev, V. N. *Int. J. Hydrogen Energy* **2006**, *31*, 171.
(33) Pintado, S.; Goberna-Ferron, S.; Escudero-Adan, E. C.; Galan-Mascaros, J. R. *J. Am. Chem. Soc.* **2013**, *135*, 13270.
(34) Goberna-Ferrón, S.; Hernández, W. Y.; Rodríguez-García, B.; Galán-Mascarós, J. R. *ACS Catal.* **2014**, *4*, 1637.
(35) Aguila, D.; Prado, Y.; Koumousi, E. S.; Mathoniere, C.; Clerac, R. *Chem. Soc. Rev.* **2016**, *45*, 203.
(36) Wang, Y.; Zhong, H.; Hu, L.; Yan, N.; Hu, H.; Chen, Q. *J. Mater. Chem. A* **2013**, *1*, 2621.
(37) Asakura, D.; Li, C. H.; Mizuno, Y.; Okubo, M.; Zhou, H.; Talham, D. R. *J. Am. Chem. Soc.* **2013**, *135*, 2793.
(38) Xie, X.; Ye, M.; Liu, C.; Hsu, P.-C.; Criddle, C. S.; Cui, Y. *Energy Environ. Sci.* **2015**, *8*, 546.
(39) Li, W.-J.; Chou, S.-L.; Wang, J.-Z.; Wang, J.-L.; Gu, Q.-F.; Liu, H.-K.; Dou, S.-X. *Nano Energy* **2015**, *13*, 200.
(40) Yue, Y.; Binder, A. J.; Guo, B.; Zhang, Z.; Qiao, Z. A.; Tian, C.; Dai, S. *Angew. Chem., Int. Ed.* **2014**, *53*, 3134.
(41) Lee, H. W.; Wang, R. Y.; Pasta, M.; Woo Lee, S.; Liu, N.; Cui, Y. *Nat. Commun.* **2014**, *5*, 5280.
(42) Wang, J.; Zhang, L.; Yu, L.; Jiao, Z.; Xie, H.; Lou, X. W.; Sun, X. W. *Nat. Commun.* **2014**, *5*, 4921.
(43) Han, L.; Bai, L.; Dong, S. *Chem. Commun.* **2014**, *50*, 802.
(44) Sekretaryova, A. N.; Beni, V.; Eriksson, M.; Karyakin, A. A.; Turner, A. P.; Vagin, M. Y. *Anal. Chem.* **2014**, *86*, 9540.
(45) Bernal, S.; Botana, F. J.; Calvino, J. J.; López-Cartes, C.; Pérez-Omil, J. A.; Rodríguez-Izquierdo, J. M. *Ultramicroscopy* **1998**, *72*, 135.
(46) Grillo, V.; Rossi, F. *Ultramicroscopy* **2013**, *125*, 112.
(47) Grillo, V.; Rotunno, E. *Ultramicroscopy* **2013**, *125*, 97.
(48) Fujita, T.; Guan, P.; McKenna, K.; Lang, X.; Hirata, A.; Zhang, L.; Tokunaga, T.; Arai, S.; Yamamoto, Y.; Tanaka, N.; Ishikawa, Y.; Asao, N.; Yamamoto, Y.; Erlebacher, J.; Chen, M. *Nat. Mater.* **2012**, *11*, 775.
(49) Itoi, M.; Jike, T.; Nishio-Hamane, D.; Udagawa, S.; Tsuda, T.; Kuwabata, S.; Boukheddaden, K.; Andrus, M. J.; Talham, D. R. *J. Am. Chem. Soc.* **2015**, *137*, 14686.
(50) Morales-Guio, C. G.; Liardet, L.; Hu, X. *J. Am. Chem. Soc.* **2016**, *138*, 8946.
(51) Cummings, C. Y.; Marken, F.; Peter, L. M.; Upul Wijayantha, K. G.; Tahir, A. A. *J. Am. Chem. Soc.* **2012**, *134*, 1228.
(52) Papaderakis, A.; Tsiplakides, D.; Balomenou, S.; Sotiropoulos, S. *J. Electroanal. Chem.* **2015**, *757*, 216.
(53) Doyle, R. L.; Lyons, M. E. *Phys. Chem. Chem. Phys.* **2013**, *15*, 5224.
(54) Lyons, M. E. G.; Brandon, M. P. *Int. J. Electrochem. Sci.* **2008**, *3*, 1386.
(55) Zhang, M.; de Respinis, M.; Frei, H. *Nat. Chem.* **2014**, *6*, 362.
(56) Murakami, M.; Hong, D.; Suenobu, T.; Yamaguchi, S.; Ogura, T.; Fukuzumi, S. *J. Am. Chem. Soc.* **2011**, *133*, 11605.
(57) Pizzolato, E.; Natali, M.; Posocco, B.; Montellano Lopez, A.; Bazzan, I.; Di Valentin, M.; Galloni, P.; Conte, V.; Bonchio, M.; Scandola, F.; Sartorel, A. *Chem. Commun.* **2013**, *49*, 9941.

DOI: 10.1021/jacs.6b09778
J. Am. Chem. Soc. 2016, 138, 16037−16045